

# Nano-island-encapsulated cobalt single-atom catalysts for breaking activity-stability trade-off in Fenton-like reactions

Received: 28 June 2024

Accepted: 18 December 2024

Published online: 02 January 2025

Check for updates

Zhi-Quan Zhang<sup>1,4</sup>, Pi-Jun Duan<sup>1,4</sup>, Jie-Xuan Zheng<sup>2</sup>, Yun-Qiu Xie<sup>1</sup>, Chang-Wei Bai<sup>1</sup>, Yi-Jiao Sun<sup>1</sup>, Xin-Jia Chen<sup>1</sup>, Fei Chen<sup>1</sup>✉ & Han-Qing Yu<sup>3</sup>✉

Single-atom catalysts (SACs) have been increasingly acknowledged for their performance in sustainable Fenton-like catalysis. However, SACs face a trade-off between activity and stability in peroxymonosulfate (PMS)-based systems. Herein, we design a nano-island encapsulated single cobalt atom ( $\text{Co}_{\text{SA}/\text{Zn.O}^-}$  ZnO) catalyst to enhance the activity and stability of PMS activation for contaminant degradation via an “island-sea” synergistic effect. In this configuration, small carrier-based ZnO nanoparticles (the “islands”) are utilized to confine and stabilize Co single atoms. The expansive ZnO substrate (the “sea”) upholds a neutral microenvironment within the reaction system. The  $\text{Co}_{\text{SA}/\text{Zn.O}^-}$  ZnO/PMS system exhibits a remarkable selectivity in exclusively generating sulfate radicals ( $\text{SO}_4^{\cdot-}$ ), leading to a complete removal of various recalcitrant pollutants within a shorter period. Characterized by minimal leaching of active sites, robust catalytic performance, and low-toxicity decontamination, this system proves highly efficient in multiple treatment cycles and complex water matrices. The design effectively breaks the activity-stability trade-off typically associated with SACs.

Persistent organic pollutants in wastewater present substantial risks to human health and ecosystems<sup>1–4</sup>. In recent years, the emerged heterogenous peroxymonosulfate-based advanced oxidation processes (PMS-AOPs) have gained recognition as effective means to generate reactive oxygen species (ROS) and eradicate refractory organic pollutants in wastewater<sup>5–8</sup>. Despite their potential, heterogeneous water treatment systems face significant challenges. The high cost of catalyst synthesis restricts practical applications, while the selectivity in producing highly oxidizing active species, particularly sulfate radicals ( $\text{SO}_4^{\cdot-}$ ), with a standard reduction potential ranging from 2.5 to 3.1 V, is not optimal. Additionally, these systems are susceptible to environmental variables, including pH conditions, coexisting ions, and organic matter, hindering their effective and reliable operation in practical scenarios. Consequently, developing

highly stabilized and active activators is crucial for the practicality of these systems.

SACs are anticipated to address cost and catalytic selectivity issues in PMS-AOPs, owing to their efficient utilization of metal atoms and adjustable electronic structures<sup>9–12</sup>. It has been reported that single-atom sites can achieve near-complete PMS conversion to  $^1\text{O}_2$ , although the selective generation of highly reactive  $\text{SO}_4^{\cdot-}$  was less explored. A significant limitation in the practical application of SACs is the activity-stability trade-off. The high reactivity of SACs stems from their unsaturated coordination environments<sup>13</sup>. However, this also renders them less stable in the demanding environment of PMS-AOPs. For instance, the in situ dissolution of PMS releases  $\text{H}^+$ , and the reaction between  $\text{SO}_4^{\cdot-}$  and  $\text{OH}^-$  further acidified the pH ( $\text{SO}_4^{\cdot-} + \text{OH}^- \rightarrow \cdot\text{OH} + \text{SO}_4^{2-}$ ).

<sup>1</sup>Key Laboratory of the Three Gorges Reservoir Region's Eco-Environment, Ministry of Education, College of Environment and Ecology, Chongqing University, Chongqing 400045, China. <sup>2</sup>College of Chemistry, Soochow University, Soochow 215006, China. <sup>3</sup>CAS Key Laboratory of Urban Pollutant Conversion, Department of Environmental Science and Engineering, University of Science and Technology of China, Hefei 230026, China. <sup>4</sup>These authors contributed equally: Zhi-Quan Zhang, Pi-Jun Duan. ✉ e-mail: [fchen0505@cqu.edu.cn](mailto:fchen0505@cqu.edu.cn); [hqyu@ustc.edu.cn](mailto:hqyu@ustc.edu.cn)

Under such acidic conditions, active metal centers are prone to leaching and diffusing into the water, diminishing catalytic performance and increasing water treatment risks<sup>14</sup>. Moreover, the highly oxidative ROS generated in Fenton-like processes can interact with single-atomic sites, weakening their bond with the support and leading to migration and aggregation of metal atoms. This results in performance decline and deactivation<sup>15–17</sup>. In the current SAC designs, carbon materials commonly act as supports to anchor single-atom catalytic sites. However, their role is typically limited to anchoring, and they do not actively participate in the catalytic process. This limitation hampers material utilization and fails to meet the requirements for treating complex wastewater. Thus, a constructive design methodology is imperative to address these challenges in Fenton-like catalysis.

The recent progress of nano-island systems has significantly influenced the development of innovative heterogeneous catalysts<sup>18</sup>. For example, Yang et al. developed cerium oxide nano-islands containing oxygen vacancies ( $\text{CeO}_{2-x}$ ), which served as a scaffold to guide the deposition of platinum single atoms, significantly boosting both the activity and stability in hydrogen evolution reactions (HER)<sup>19</sup>. In parallel, Zheng et al. introduced a nanoscale island confinement approach, effectively restricting active metal atoms within defined areas. This strategy led to the enhanced HER catalytic activity and durability, benefiting from the synergistic interaction between the confined islands and the surrounding matrix<sup>20</sup>. These systems feature distinct “islands” (active sites dispersed on small functional carriers) and “seas” (high-surface-area supports), each playing specific roles in catalytic reactions to address multifaceted challenges. Furthermore, nano-islands can modify metal-support interactions (MSI), thereby enhancing the stability of active metal atoms<sup>15</sup>. Developing a synergistic nano-island-sea catalytic system is anticipated to tackle the complexities of catalytic processes effectively. In Fenton-like reactions, nano-islands are envisioned as anchors for atomically dispersed metal atoms, ensuring stable selective catalysis, while the support, akin to a “sea”, maintains a neutral microenvironment for the reaction. However, studies on nano-island systems remain limited, and the inner structure-activity relationship, catalytic mechanisms, and broader applicability of these systems have not been fully elucidated yet.

With the above analyses in mind, in this work, zinc oxide (ZnO, amphoteric oxide) was selected as the foundation for constructing nano-island catalysts due to its cost-effectiveness, biocompatibility, and amphoteric nature<sup>21</sup>. We devised a one-step hydrothermal synthesis method to fabricate  $\text{Co}_{\text{SA}/\text{Zn}_n\text{O}}\text{-ZnO}$  nano-island catalysts. In this design, the surface ZnO nanoparticles (“islands”) functioned as nano-glue, confining and stabilizing Co single atoms, while the ZnO support (“sea”) could regulate the reaction pH and foster a neutral microenvironment. The  $\text{Co}_{\text{SA}/\text{Zn}_n\text{O}}\text{-ZnO/PMS}$  system’s efficacy was demonstrated by treating multiple sulfonamide antibiotics in complex water matrices. This island-sea synergistic approach achieved exceptional and stable catalytic performance, with the reaction kinetics constant for sulfamethoxazole (SMX) removal reaching  $98.2 \text{ min}^{-1} \text{ M}^{-1}$ , surpassing those in related studies. Notably, the  $\text{Co}_{\text{SA}/\text{Zn}_n\text{O}}\text{-ZnO/PMS}$  system exhibited high selectivity in generating  $\text{SO}_4^{\cdot-}$  for pollutant degradation. Theoretical calculations were further conducted to investigate the impact of monoatomic Co sites on the electronic structure and reaction thermodynamics. Further, we developed a catalytic membrane reactor to evaluate its application potential. This work provides significant insights into the design of single-atom Fenton-like catalysts and offers valuable perspectives for treating refractory wastewater.

## Results

### Characteristics of nano-island-encapsulated Co SACs

Zinc oxide (ZnO) and ZnO nano-islands encapsulating various transition metal single atoms (Co, Mn, Cu, Fe, Ni) were synthesized utilizing a

one-step hydrothermal method (Fig. 1a and Supplementary Fig. 1). Among these, the constructed  $\text{Co}_{\text{SA}/\text{Zn}_n\text{O}}\text{-ZnO}$  sample distinguished itself with a special morphological structure (Fig. 1e and Supplementary Fig. 2). The possible reason might be that the ionic radii of Co and Zn were consistent, while the other metals showed a mismatch (Supplementary Fig. 3). To provide a comparative perspective, different concentrations of Co (1%, 5%, 10%) were synthesized, where the percentage denotes the molar ratio of Co to Zn (Supplementary Figs. 4, 5 and Supplementary Table 1). The 5% Co sample was selected for in-depth study due to its optimal catalytic performance. X-ray diffraction (XRD) analysis (Fig. 1l) revealed that both ZnO and  $\text{Co}_{\text{SA}/\text{Zn}_n\text{O}}\text{-ZnO}$  maintained the wurtzite phase hexagonal crystal structure of ZnO (JCPDS No. 36-1451), with no indication of other phases. This finding underscored the high crystallinity of ZnO and the atomic-level dispersion of Co within the ZnO matrix<sup>22</sup>. Post-Co incorporation, notable shifts in the diffraction peaks at the (100), (002), and (101) planes to higher  $2\theta$  angles were found, indicative of lattice expansion. The parallelism in valence state, electron configuration, and ionic radius between  $\text{Co}^{2+}$  and  $\text{Zn}^{2+}$  led to the inference that Co was integrated into the ZnO lattice through substitutional doping, as opposed to interstitial gap doping<sup>23</sup>. The successful synthesis of  $\text{Co}_{\text{SA}/\text{Zn}_n\text{O}}\text{-ZnO}$  was further substantiated by Raman and Fourier-transform infrared (FTIR) analyses (Supplementary Figs. 6 and 7). These characterizations provided additional insights into the structural integrity and compositional purity of the targeted  $\text{Co}_{\text{SA}/\text{Zn}_n\text{O}}\text{-ZnO}$  nano-island catalysts, affirming their potential for catalytic applications.

The pristine ZnO demonstrated a smooth hexahedral structure, with a homogeneous distribution of zinc (Zn) and oxygen (O) elements (Fig. 1b–d and Supplementary Figs. 8–11). Upon the incorporation of cobalt (Co), the emergence of numerous small particles was observed on the surface of the samples (Fig. 1e and Supplementary Figs. 12–14). XRD analyses conclusively ruled out the formation of Co nanoclusters. High-resolution transmission electron microscopy (HRTEM) imaging (Supplementary Fig. 15) revealed distinct lattice fringes of these small particles, with lattice spacings of approximately 0.28 nm and 0.25 nm. These spacings correspond to the (100) and (101) crystalline facets of ZnO, confirming that the small particles were ZnO. Further analysis using high-angle annular dark-field scanning transmission electron microscopy (HAADF-STEM) elemental mapping (Fig. 1f–i and Supplementary Fig. 16) revealed the presence of Zn, Co, and O in the  $\text{Co}_{\text{SA}/\text{Zn}_n\text{O}}\text{-ZnO}$  samples. Notably, Co was highlighted on the flanks of the substrate, a phenomenon suggesting an overlap from top to bottom. This observation provided insights into the distribution of Co sites on these small particles. To elucidate the form of Co on small particle surfaces, the HAADF-STEM was utilized (Fig. 1k and Supplementary Fig. 17). The imaging revealed individual Co atoms, highlighted by red circles, affirming their discrete atomic presence. Additionally, elemental analysis was conducted on two specific areas of the catalyst surface (Fig. 1j). At location 3, no Co signal peak was detected, implying negligible Co content. In contrast, at location 4, a pronounced Co signal was detected, indicating a substantial concentration of 5.7 wt% (Fig. 1j and Supplementary Fig. 18), further suggesting the presence of Co SAs on the small surface particles. This finding robustly affirms the successful fabrication of  $\text{Co}_{\text{SA}/\text{Zn}_n\text{O}}\text{-ZnO}$  nano-island catalysts. X-ray photoelectron spectroscopy (XPS) (Supplementary Fig. 19) was employed to further characterize the valence states of the incorporated elements. The high-resolution XPS spectrum of Co 2p displayed peaks at 779.8 eV and 781.2 eV, corresponding to the oxidation states of  $\text{Co}^{3+}$  and  $\text{Co}^{2+}$ , respectively<sup>24</sup>. This provided compelling evidence that Co atoms were successfully integrated into the ZnO lattice, reinforcing the nano-island structure of the  $\text{Co}_{\text{SA}/\text{Zn}_n\text{O}}\text{-ZnO}$  catalysts.

To examine the valence and coordination environment of Co sites in the  $\text{Co}_{\text{SA}/\text{Zn}_n\text{O}}\text{-ZnO}$  sample, comprehensive X-ray absorption fine structure (XAFS) analyses were conducted. The Co-K-edge X-ray absorption near-edge structure (XANES) spectra, displayed in

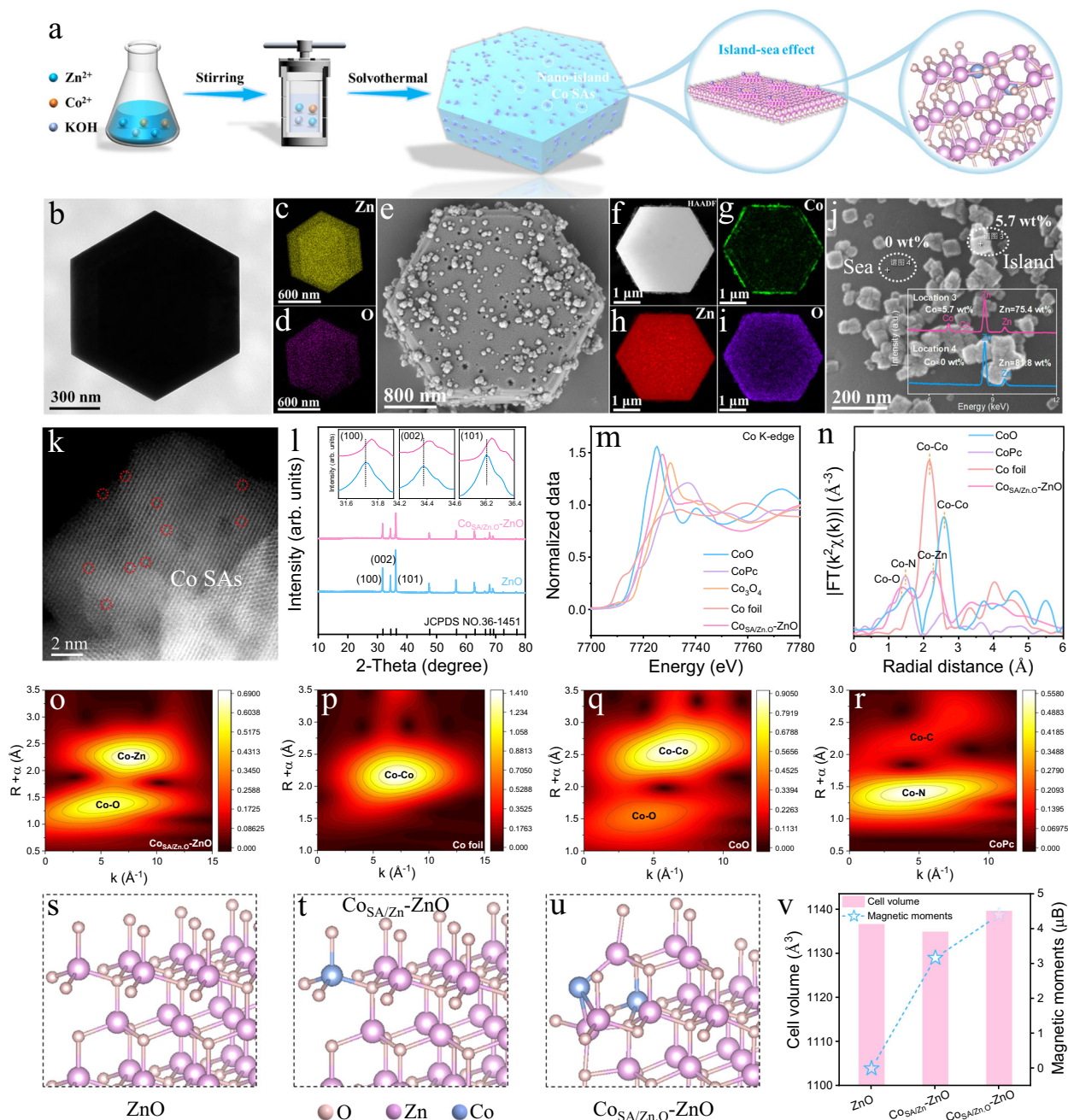


**Fig. 1 | Validation of nano-island structure of Co SAs.** **a** Synthesis procedure of  $\text{Co}_{\text{SA/ZnO}}\text{-ZnO}$ . **b** TEM image of ZnO. TEM elemental mappings of ZnO with (c) Zn and (d) O. **e** SEM image of  $\text{Co}_{\text{SA/ZnO}}\text{-ZnO}$ . HAADF-STEM elemental mappings of  $\text{Co}_{\text{SA/ZnO}}\text{-ZnO}$  with (f) original, (g) Co, (h) Zn, and (i) O. **j** SEM image of small particles on the surface of  $\text{Co}_{\text{SA/ZnO}}\text{-ZnO}$  (inset: distribution of Co content in different locations of  $\text{Co}_{\text{SA/ZnO}}\text{-ZnO}$  catalyst). **k** HAADF-STEM image of  $\text{Co}_{\text{SA/ZnO}}\text{-ZnO}$  (Co SAs marked by red circles). **l** XRD pattern of ZnO and  $\text{Co}_{\text{SA/ZnO}}\text{-ZnO}$  (inset:

enlarged view of (100), (002) and (101) crystal facets). **m** XANES spectra of  $\text{Co}_{\text{SA/ZnO}}\text{-ZnO}$  at the Co K-edge. **n** FT  $k_3$ -weighted EXAFS spectra of  $\text{Co}_{\text{SA/ZnO}}\text{-ZnO}$  and references. WT-EXAFS for K-edge for (o)  $\text{Co}_{\text{SA/ZnO}}\text{-ZnO}$ , (p) Co foil, (q) CoO and (r) CoPc. Three configurations of (s) monomer ZnO, (t) Co replaced Zn and (u) Co replaced Zn, O. **v** Comparison of cell volume and magnetic moment of three configurations.

Fig. 1m, reveal that the absorption edge of Co atoms in  $\text{Co}_{\text{SA/ZnO}}\text{-ZnO}$  lies intermediate to that of CoO and  $\text{Co}_3\text{O}_4$ . This positioning suggests that the Co atoms exhibited a mixed valence state, oscillating between +2 and +3<sup>25</sup>. Additionally, the Fourier Transform Extended X-ray Absorption Fine Structures (FT-EXAFS) analysis (Fig. 1n) identifies two pronounced peaks at 2.28 Å and 1.38 Å, corresponding to Co-Zn and Co-O coordination, respectively. Moreover, the absence of a Co-Co peak in these spectra confirmed the lack of Co clusters within the  $\text{Co}_{\text{SA/ZnO}}\text{-ZnO}$  structure<sup>24,26,27</sup>. Wavelet transform (WT)-EXAFS results (Fig. 1o–r) further delineate two distinct peaks at 7.6 and 5.5 Å<sup>-1</sup>,

attributed to the Co-Zn and Co-O shells in  $\text{Co}_{\text{SA/ZnO}}\text{-ZnO}$ , respectively. Again, the absence of Co-Co peaks corroborated the atomic dispersion of Co sites within the structure<sup>28–30</sup>. Quantitative least squares EXAFS curve fitting (Supplementary Fig. 21 and Supplementary Table 2) provided additional insights into the structural parameters of Co atoms. The result indicated Co atoms were coordinated with both O and Zn atoms, exhibiting coordination numbers of 3.2 and 3.1, and bond lengths of 1.89 Å and 2.40 Å, respectively. This finding suggests that Co atoms replaced both Zn and O atoms in the lattice. Theoretical computational analysis was conducted to substantiate these findings,

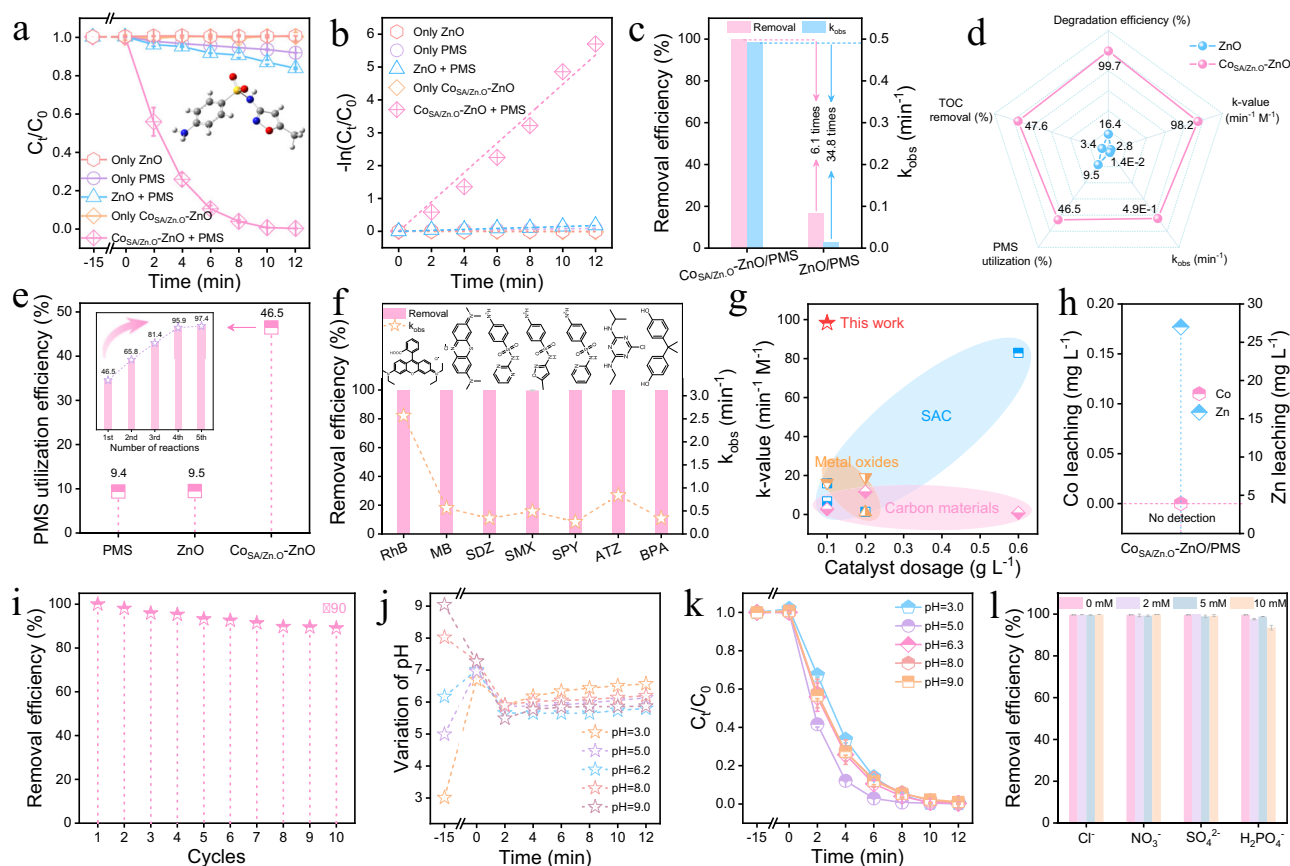


**Fig. 2 | Efficient and self-pH-stable Fenton-like decontamination.** **a** Degradation rates of SMX with different reaction systems (inset: the molecular model of SMX). **b** The corresponding reaction rate constants in different reaction systems (Conditions:  $[\text{Catal.}]_0 = 0.1 \text{ g L}^{-1}$ ,  $[\text{PMS}]_0 = 0.5 \text{ mM}$ ,  $[\text{pH}]_0 = 6.3$ ,  $[\text{SMX}]_0 = 10 \text{ mg L}^{-1}$ ,  $[\text{Temp.}] = 20 \pm 2 \text{ }^\circ\text{C}$ ). Degradation kinetics data were fitted using a first-order equation. **c** Comparison of degradation efficiencies and reaction rate constants of ZnO and  $\text{Co}_{\text{SA}/\text{Zn}_2\text{O}}$ -ZnO. **d** Comparison of various parameters of ZnO and  $\text{Co}_{\text{SA}/\text{Zn}_2\text{O}}$ -ZnO. **e** Comparison of PMS utilization efficiencies of ZnO and  $\text{Co}_{\text{SA}/\text{Zn}_2\text{O}}$ -ZnO (inset: utilization of PMS for five consecutive reactions). **f** Removal of multiple pollutants

by  $\text{Co}_{\text{SA}/\text{Zn}_2\text{O}}$ -ZnO/PMS reaction system. **g** Comparison of  $k$ -values for SMX removal with reported materials. **h** Leakage of Co and Zn ions after  $\text{Co}_{\text{SA}/\text{Zn}_2\text{O}}$ -ZnO/PMS system reaction. **i** Evaluation of SMX removal using  $\text{Co}_{\text{SA}/\text{Zn}_2\text{O}}$ -ZnO/PMS system with ten cycles. **j** Variation of pH value of  $\text{Co}_{\text{SA}/\text{Zn}_2\text{O}}$ -ZnO/PMS reaction system under different initial pH conditions. **k** Degradation efficiency of SMX by  $\text{Co}_{\text{SA}/\text{Zn}_2\text{O}}$ -ZnO/PMS system at different initial pH. **l** Effect of background ions on  $\text{Co}_{\text{SA}/\text{Zn}_2\text{O}}$ -ZnO/PMS reaction system. The error bars represent the standard deviation of three replicate tests.

which involved constructing models of pristine ZnO, Co substituted for Zn ( $\text{Co}_{\text{SA}/\text{Zn}}$ -ZnO), and Co substituting both Zn and O ( $\text{Co}_{\text{SA}/\text{Zn}_2\text{O}}$ -ZnO) (Fig. 1s–u). The results indicate that Co's bond lengths and coordination numbers in the  $\text{Co}_{\text{SA}/\text{Zn}_2\text{O}}$ -ZnO configuration align closely with the EXAFS curve fitting data. Additionally, the cell volume of these configurations (Fig. 1v and Supplementary Table 3), revealed that the Co substitution for both O and Zn results in the largest cell volume, corroborating the XRD findings. This result implies that such a configuration could facilitate an active electronic state conducive to Fenton-like catalysis. Therefore, these analyses indicate that the  $\text{Co}_{\text{SA}/\text{Zn}_2\text{O}}$ -ZnO catalyst featured a nano-island structure, with single-atom Co sites dispersed on ZnO "islands", underscoring its potential as an effective catalyst in Fenton-like processes.

### Catalytic activity and stability of the "island-sea" Fenton-like reactor

In this study, the broad-spectrum antimicrobial drug SMX was chosen as the target pollutant to evaluate the efficacy of various catalysts in activating PMS for degradation purposes. Firstly, the performance of different MSA-ZnO (Co, Mn, Cu, Fe, Ni) catalysts in activating PMS for the degradation of SMX was compared. The performance assessment (Supplementary Figs. 22, 23 and Supplementary Tables 4, 5) demonstrated that the  $\text{Co}_{\text{SA}/\text{Zn}_2\text{O}}$ -ZnO catalyst showed exceptional degradation capabilities, achieving almost complete (100%) removal of SMX

within just 12 min. This performance confirmed the effectiveness of Co as a catalyst for PMS activation. Furthermore, among the tested MSA-ZnO catalysts, only the  $\text{Co}_{\text{SA}/\text{Zn}_2\text{O}}$ -ZnO featured a distinctive nano-island configuration, which significantly enhanced the activation of PMS for SMX degradation. Additionally, an investigation into the optimal Co ratio demonstrated that a 5% Co concentration yielded the most effective degradation performance. Optimal conditions were determined with the  $\text{Co}_{\text{SA}/\text{Zn}_2\text{O}}$ -ZnO and PMS concentration set at  $0.1 \text{ g L}^{-1}$  and  $0.5 \text{ mM}$ , respectively (Supplementary Figs. 26–28 and Supplementary Table 8). Comparative experiments (Fig. 2a and Supplementary Table 9) suggested that the adsorption of SMX on both  $\text{Co}_{\text{SA}/\text{Zn}_2\text{O}}$ -ZnO and ZnO was minimal. It was observed that PMS alone accounted for only an 8.3% reduction in SMX concentration over 12 min. In contrast, the ZnO/PMS system achieved a 16.4% SMX removal. Remarkably, the  $\text{Co}_{\text{SA}/\text{Zn}_2\text{O}}$ -ZnO/PMS system outperformed the standalone ZnO and PMS systems, achieving a 99.7% removal, which was approximately 6.1 and 12.0 times greater, respectively. The kinetic analysis of the reaction followed pseudo-first-order kinetics. The observed kinetic constant ( $k_{\text{obs}}$ ) for the  $\text{Co}_{\text{SA}/\text{Zn}_2\text{O}}$ -ZnO/PMS system was significantly higher ( $k_{\text{obs}} = 0.491 \text{ min}^{-1}$ ) compared to the ZnO/PMS ( $k_{\text{obs}} = 0.014 \text{ min}^{-1}$ ) and PMS alone ( $k_{\text{obs}} = 0.007 \text{ min}^{-1}$ ) system (Fig. 2b, c). To further assess the efficiency of the  $\text{Co}_{\text{SA}/\text{Zn}_2\text{O}}$ -ZnO catalyst, comparisons of  $k_{\text{obs}}$  were conducted with other reported Co-based catalysts (Supplementary Table 10). The obtained results

indicated that  $\text{Co}_{\text{SA}/\text{Zn}_2\text{O}}\text{-ZnO}$  catalyst achieved the highest  $k_{\text{obs}}$  value, emphasizing its superior capability in activating PMS, thereby enhancing the degradation of SMX. Furthermore, a comprehensive evaluation of the degradation performance among 14 different catalysts, including CoO and  $\text{Co}_3\text{O}_4$ , was carried out (Supplementary Fig. 29 and Supplementary Table 11). Within this group, the  $\text{Co}_{\text{SA}/\text{Zn}_2\text{O}}\text{-ZnO}$  still exhibited the highest  $k_{\text{obs}}$  value. These findings unequivocally confirmed the exceptional catalytic performance of the  $\text{Co}_{\text{SA}/\text{Zn}_2\text{O}}\text{-ZnO/PMS}$  system.

To evaluate the efficiency of PMS utilization among various catalysts, PMS consumption was meticulously quantified. As depicted in Fig. 2e, the  $\text{Co}_{\text{SA}/\text{Zn}_2\text{O}}\text{-ZnO}$  catalyst exhibited a PMS utilization of 46.7% over a 12-min reaction. This rate notably exceeded the performances of ZnO (9.5%) and PMS alone (9.4%) by factors of 4.90 and 4.95, respectively. Furthermore, the  $\text{Co}_{\text{SA}/\text{Zn}_2\text{O}}\text{-ZnO}$  catalyst maintained a high utilization efficiency of 97.5% even after five reaction cycles, demonstrating its robust capability for sustained PMS activation. Additionally, the constructed  $\text{Co}_{\text{SA}/\text{Zn}_2\text{O}}\text{-ZnO/PMS}$  system demonstrated a significant enhancement in total organic carbon (TOC) removal (Fig. 2d). The system could achieve a high mineralization rate of 47.6% for SMX within 12 min, substantially higher than the 3.4% achieved by the ZnO/PMS system. The versatile efficacy of the  $\text{Co}_{\text{SA}/\text{Zn}_2\text{O}}\text{-ZnO/PMS}$  system was further corroborated by its complete removal of a range of pollutants, including rhodamine B (RhB), methylene blue (MB), sulfadiazine (SDZ), sulfapyridine (SPY), atrazine (ATZ), and bisphenol A (BPA) (Fig. 2f, Supplementary Figs. 31–33 and Supplementary Table 12). Notably, the system's observed  $k_{\text{obs}}$  for SMX removal reached  $98.2 \text{ min}^{-1} \text{ M}^{-1}$ , almost the highest among all surveyed catalysts (Fig. 2g and Supplementary Table 13). These findings compellingly demonstrated the superior decontamination capability of the  $\text{Co}_{\text{SA}/\text{Zn}_2\text{O}}\text{-ZnO/PMS}$  system against both electron-rich and electron-deficient pollutants.

Moreover, the nano-island structure of the  $\text{Co}_{\text{SA}/\text{Zn}_2\text{O}}\text{-ZnO}$  catalyst contributed to its exceptional stability, maintaining about 90% SMX removal efficiency even after ten reaction cycles (Fig. 2i). This durability could be attributed to the firmly anchored, atomically dispersed Co atoms on the nano-islands, which resisted detachment during PMS activation. Additionally, the amphoteric nature of ZnO played a crucial role in maintaining a neutral microenvironment within the reaction system, thereby enhancing stability (Supplementary Figs. 34 and 35). To substantiate this hypothesis, real-time monitoring of pH variations was conducted across different initial pH values, with results presented in Fig. 2j. These findings indicate the system's ability to maintain a near-neutral pH (-6.1), irrespective of the solution's initial acidic or alkaline nature. This pH regulation contributed to the system's superior degradation performance across a wide initial pH range (3.0 to 9.0) (Fig. 2k and Supplementary Table 14). In terms of metal ion leakage, the system demonstrated no detectable leakage of Co ions ( $0 \text{ mg L}^{-1}$ ) (Fig. 2h and Supplementary Fig. 36). However, a leakage of zinc ions was observed at approximately  $27 \text{ mg L}^{-1}$ , affirming the presence of an island-sea synergistic effect. This effect was hypothesized to arise from ZnO precipitating  $\text{Zn}^{2+}$  ions, thereby sustaining a neutral microenvironment and concurrently minimizing Co leakage<sup>31</sup>. The effect of temperature on the degradation of SMX by  $\text{Co}_{\text{SA}/\text{Zn}_2\text{O}}\text{-ZnO/PMS}$  system indicated that the system had a wide temperature tolerance range (Supplementary Fig. 39). And the activation energy ( $E_a$ ) values of  $8.21 \text{ kJ mol}^{-1}$  and  $33.33 \text{ kJ mol}^{-1}$  were quantified for SMX removal in the  $\text{Co}_{\text{SA}/\text{Zn}_2\text{O}}\text{-ZnO/PMS}$  and ZnO/PMS systems, respectively, suggesting that PMS activation was more prone to occur on nano-island  $\text{Co}_{\text{SA}/\text{Zn}_2\text{O}}\text{-ZnO}$  catalyst. Furthermore, the  $\text{Co}_{\text{SA}/\text{Zn}_2\text{O}}\text{-ZnO/PMS}$  system's performance remained robust in various inorganic ions and organic compounds. The coexistence of anions like nitrate ( $\text{NO}_3^-$ ), chloride ( $\text{Cl}^-$ ), sulfate ( $\text{SO}_4^{2-}$ ), and dihydrogen phosphate ( $\text{H}_2\text{PO}_4^-$ ), as well as humic acids (HA), had negligible impact on SMX removal (Fig. 2l, Supplementary Figs. 40–44 and Supplementary Table 15). This

observation demonstrates such a catalytic system's capacity to effectively eliminate diverse pollutants in complex water matrices.

Overall, these results demonstrate that the nano-island structure design effectively enhanced the catalyst's stability and activity, successfully overcoming the common trade-off between activity and stability in SAC catalysis. This approach positions the  $\text{Co}_{\text{SA}/\text{Zn}_2\text{O}}\text{-ZnO/PMS}$  system as a highly efficient pollutant degradation approach in different scenarios.

### Main active species involved in the catalytic reaction

To elucidate the primary active species driving the reaction in the  $\text{Co}_{\text{SA}/\text{Zn}_2\text{O}}\text{-ZnO/PMS}$  system, various scavengers were employed: *tert*-butyl alcohol (TBA) for hydroxyl radicals ( $\cdot\text{OH}$ ), methanol (MeOH) for sulfate radicals ( $\text{SO}_4^{\cdot-}$ ), TEMPOL for superoxide radicals ( $\text{O}_2^{\cdot-}$ ), and *L*-histidine for singlet oxygen ( $^1\text{O}_2$ ) (Fig. 3a)<sup>32–35</sup>. The negligible impact of TBA addition on degradation efficiency implies that  $\cdot\text{OH}$  might not be the dominant active species. Conversely, the substantial inhibition of degradation upon introducing MeOH, TEMPOL, and *L*-histidine suggests the possible presence of  $\text{SO}_4^{\cdot-}$ ,  $\text{O}_2^{\cdot-}$ , and  $^1\text{O}_2$  in the system. To corroborate these findings, electron spin resonance (ESR) measurements were performed. As shown in Fig. 3b, a distinct ESR signal characteristic of the  $\text{SO}_4^{\cdot-}$  radical (1:1:1:1:1) was observed<sup>36</sup>, with its intensity increasing over time. The absence of a signal for  $\cdot\text{OH}$  in ESR spectra provided compelling evidence that  $\text{SO}_4^{\cdot-}$  was the principal active species, aligning with the results of radical scavenging experiments. Furthermore, ESR spectra characterized signals of  $\text{TEMP}\cdot^1\text{O}_2$  and  $\text{DMPO}\cdot\text{O}_2^{\cdot-}$  in the  $\text{Co}_{\text{SA}/\text{Zn}_2\text{O}}\text{-ZnO/PMS}$  system (Fig. 3c and Supplementary Fig. 45) showed a characterized signal of  $\text{TEMP}\cdot^1\text{O}_2$  and  $\text{DMPO}\cdot\text{O}_2^{\cdot-}$  in the  $\text{Co}_{\text{SA}/\text{Zn}_2\text{O}}\text{-ZnO/PMS}$  system, indicating the possible generation of  $^1\text{O}_2$  and  $\text{O}_2^{\cdot-}$ . Subsequent experiments replacing  $\text{H}_2\text{O}$  with deuterium oxide ( $\text{D}_2\text{O}$ ) (Supplementary Fig. 46) revealed only a slight increase in the degradation rate, implying the formation of  $^1\text{O}_2$  only as an auxiliary role<sup>37</sup>. Nitrotetrazolium blue chloride (NBT) probe experiments (Supplementary Fig. 47) demonstrated the minimal generation of  $\text{O}_2^{\cdot-}$ <sup>38</sup>, and the limited conversion from  $\text{PMSO}$  to  $\text{PMSO}_2$  further confirmed the absence of relevant high-valent Co species (Supplementary Fig. 48). Moreover, quantification of the contributions of different species was conducted using benzoic acid (BA) and nitrobenzene (NB) probes (Supplementary Figs. 49 and 50). These analyses revealed that the steady-state concentration of  $\text{SO}_4^{\cdot-}$  was an order of magnitude higher than that of  $\cdot\text{OH}$  (Supplementary Fig. 51). Calculations based on Eqs. (S1)–(S8) indicate that  $\text{SO}_4^{\cdot-}$  contributed 96.3% to the reaction, with  $\cdot\text{OH}$  and  $^1\text{O}_2$  contributing only 3.7% (Fig. 3d). These findings robustly confirm that  $\text{SO}_4^{\cdot-}$  was the predominant species responsible for the enhanced degradation performance in the  $\text{Co}_{\text{SA}/\text{Zn}_2\text{O}}\text{-ZnO/PMS}$  system. The results of the quenching experiments of the  $\text{Co}_{\text{SA}/\text{Zn}_2\text{O}}\text{-ZnO/PMS}$  at varying pH levels and sulfonamide contaminants align with the above findings (Supplementary Figs. 52–61 and Supplementary Tables 16, 17). Overall, all of the experimental findings outlined above indicated the potential pitfalls of relying exclusively on individual validation methods, which could lead to misinterpretations. This emphasized the necessity of adopting a comprehensive approach that integrated multiple analytical techniques to accurately determine both the formation and activity of reactive species within catalytic systems.

Electrochemical impedance spectra (EIS) and cyclic voltammetry (CV) analyses revealed that the  $\text{Co}_{\text{SA}/\text{Zn}_2\text{O}}\text{-ZnO}$  exhibited lower charge transfer resistance and higher specific capacitance (Fig. 3e, f)<sup>39,40</sup>. This indicated the enhanced catalytic activity afforded by the nano-island architecture of  $\text{Co}_{\text{SA}/\text{Zn}_2\text{O}}\text{-ZnO}$ . Linear sweep voltammetry (LSV) was used to evaluate the kinetics of electron transfer<sup>41</sup>, where the current density for the  $\text{Co}_{\text{SA}/\text{Zn}_2\text{O}}\text{-ZnO}$  electrode was substantially greater than that of ZnO (Fig. 3e), signifying more rapid electron transfer. The *i*-*t* curves (Fig. 3g), derived from chronoamperometry studies, provided insight into the electron transfer pathway<sup>42–44</sup>. Upon the addition of

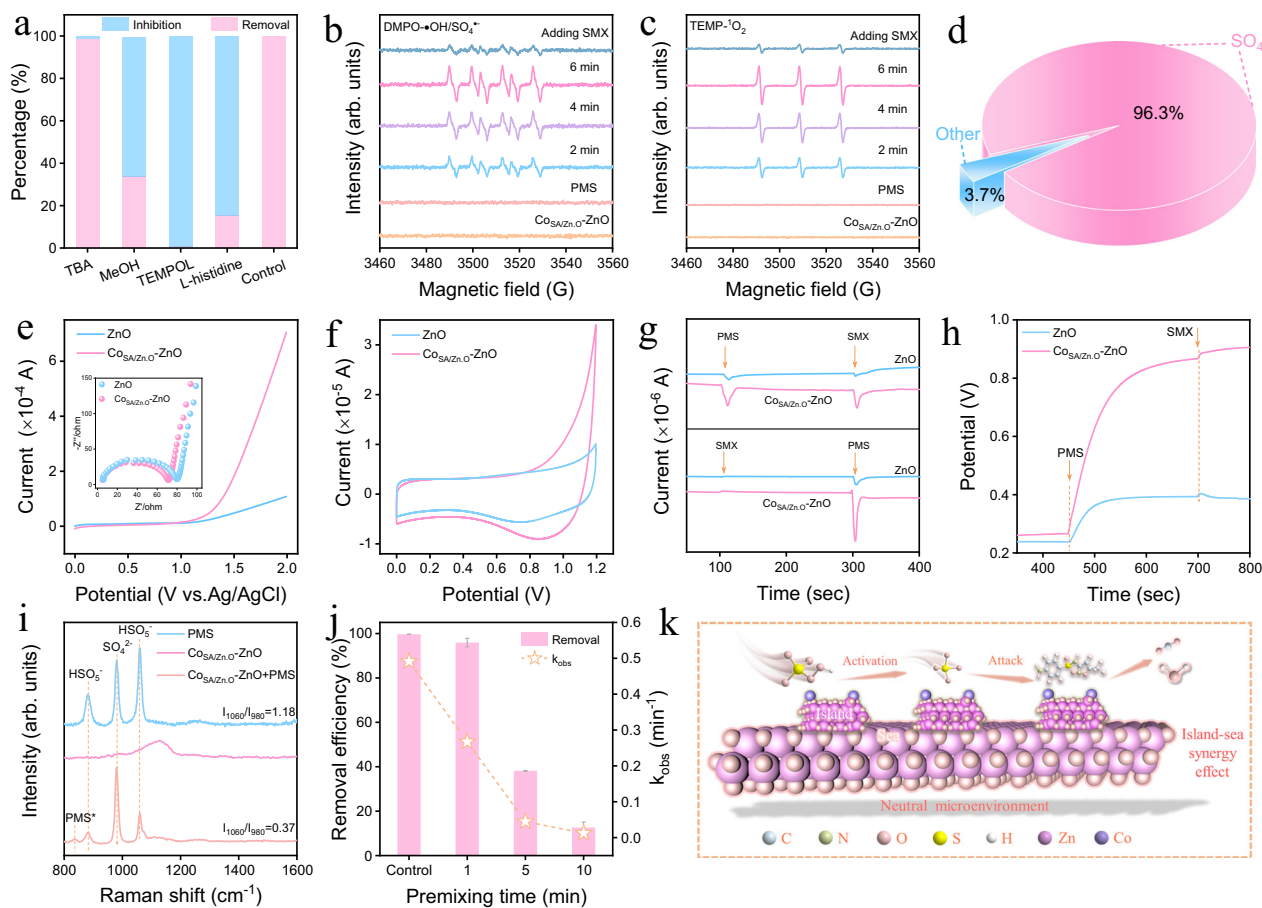


**Fig. 3 | Identification of the primary reactive species.** **a** Degradation of SMX in the presence of various scavengers in the  $\text{Co}_{\text{SA}/\text{Zn}_2\text{O}}\text{-ZnO}/\text{PMS}$  system. **b** DMPO spin-trapping ESR spectra for  $\text{DMPO}\cdot\text{OH}/\text{SO}_4^{\cdot-}$  in the  $\text{Co}_{\text{SA}/\text{Zn}_2\text{O}}\text{-ZnO}/\text{PMS}$  system. **c** TEMP-based ESR spectra for  $^1\text{O}_2$  in the  $\text{Co}_{\text{SA}/\text{Zn}_2\text{O}}\text{-ZnO}/\text{PMS}$  system. **d** The proportion of active species in the  $\text{Co}_{\text{SA}/\text{Zn}_2\text{O}}\text{-ZnO}/\text{PMS}$  system. **e** LSV curves of ZnO and  $\text{Co}_{\text{SA}/\text{Zn}_2\text{O}}\text{-ZnO}$  electrodes (inset: EIS spectra of ZnO and  $\text{Co}_{\text{SA}/\text{Zn}_2\text{O}}\text{-ZnO}$ ). **f** Cyclic voltammetric curves of ZnO and  $\text{Co}_{\text{SA}/\text{Zn}_2\text{O}}\text{-ZnO}$  electrodes. **g** Amperometric  $i$ - $t$  curve

measurements upon the addition of PMS and SMX using ZnO and  $\text{Co}_{\text{SA}/\text{Zn}_2\text{O}}\text{-ZnO}$  as the working electrode. **h** Open-circuit potential of ZnO and  $\text{Co}_{\text{SA}/\text{Zn}_2\text{O}}\text{-ZnO}$ . **i** In situ Raman spectra of different reaction systems. **j** The effect of pre-mixing time on SMX removal in the  $\text{Co}_{\text{SA}/\text{Zn}_2\text{O}}\text{-ZnO}/\text{PMS}$  system. The error bars represent the standard deviation of three replicate tests. **k** Reaction mechanisms in the  $\text{Co}_{\text{SA}/\text{Zn}_2\text{O}}\text{-ZnO}/\text{PMS}$  system.

PMS, a discernible decline in current density for  $\text{Co}_{\text{SA}/\text{Zn}_2\text{O}}\text{-ZnO}$  was noted, suggesting electron redistribution due to PMS interaction with catalytic sites<sup>45</sup>. Conversely, the addition of SMX prompted negligible changes, confirming the role of PMS in active complex formation for  $\text{SO}_4^{\cdot-}$  generation<sup>8</sup>. Further analysis involved open-circuit potential monitoring and pre-mixing experiments (Fig. 3h, j and Supplementary Fig. 64), which showed an immediate potential increase on  $\text{Co}_{\text{SA}/\text{Zn}_2\text{O}}\text{-ZnO}$  and ZnO electrodes upon PMS addition, indicative of active PMS complex formation on the catalyst surface. The absence of potential decrease post-SMX addition negated the involvement of catalyst-mediated electron transfer processes (ETP). Pre-mixing experiments, wherein  $\text{Co}_{\text{SA}/\text{Zn}_2\text{O}}\text{-ZnO}$  was combined with PMS prior to SMX addition, revealed a decline in SMX removal efficiency with increasing pre-mixing time. This supported the hypothesis that PMS, in the absence of SMX, rapidly decomposed to generate  $\text{SO}_4^{\cdot-}$  and the ETP mechanism was also ruled out (Fig. 3j). In situ Raman spectroscopy (Fig. 3i), was utilized to track PMS adsorption and evolution on the  $\text{Co}_{\text{SA}/\text{Zn}_2\text{O}}\text{-ZnO}$  surface. The identified peaks at 885 and 1060  $\text{cm}^{-1}$  were ascribed to  $\text{HSO}_5^{\cdot}$  in PMS, while the 980  $\text{cm}^{-1}$  peak likely corresponds to the S=O bond stretching vibration in  $\text{SO}_4^{2-}$ . Upon introduction of PMS to  $\text{Co}_{\text{SA}/\text{Zn}_2\text{O}}\text{-ZnO}$ , a new peak at 834  $\text{cm}^{-1}$  emerged, denoting the formation of reactive peroxides (PMS), which are instrumental in O-O bond cleavage for  $\text{SO}_4^{\cdot-}$  generation. This observation corroborates the electrochemical findings. Furthermore, the  $I_{1060}/I_{980}$  ratio, a potential

indicator of PMS consumption, initially stood at 1.18 for PMS alone but decreased to 0.37 and 0.28 as the reaction progressed in the  $\text{Co}_{\text{SA}/\text{Zn}_2\text{O}}\text{-ZnO}/\text{PMS}$  system (Fig. 3i and Supplementary Fig. 65). This result suggests that electron transfer from  $\text{Co}_{\text{SA}/\text{Zn}_2\text{O}}\text{-ZnO}$  to PMS favored the generation of  $\text{SO}_4^{\cdot-}$ , reinforcing the efficacy of the catalyst's nano-island structure in promoting AOPs.

The above results indicate that Co SACs with a nano-island-sea configuration were successfully developed, enhancing both high stability and activity, and significantly breaking the bottleneck of traditional SAC-based AOPs. The “islands” in this design effectively confined and dispersed single-atom Co sites, while the ZnO “sea” maintained a neutral microenvironment, crucial for the catalytic reaction. This “island-sea” synergy facilitated a highly efficient and robust reaction, capable of selectively generating  $\text{SO}_4^{\cdot-}$ , thus comprehensively removing a wide range of pollutants and resolving the prevalent activity-stability trade-off in SACs (Fig. 3k).

### Mechanisms for the high performance of the “nano-island-sea” system

Theoretical calculations could provide deep insights into the remarkable Fenton-like activity exhibited by the nano-island encapsulated single-atom Co catalysts. The initial investigations focused on the impact of single Co atom incorporation on the ZnO surface, specifically examining charge density symmetry and active site exposure.

Charge density distribution and electrostatic potential on the pristine ZnO surface displayed notable symmetry (Fig. 4a and Supplementary Fig. 66). The substitution of Zn atoms with Co atoms on the ZnO surface led to a discernible decline in charge density at the Co sites and a significant reduction in electrostatic potential. This alteration suggests that Co doping disrupted the surface's symmetric charge distribution and generated additional reactive sites, thereby enhancing the adsorption and activation of reactants, which was favored for both PMS adsorption and O-O bond dissociation.

Moreover, we computed the work functions of three distinct structures to reveal significant changes upon introducing a single Co atom site (Fig. 4c and Supplementary Fig. 67). The presence of a single Co atom notably elevated the Fermi energy level ( $E_{\text{fermi}}$ ) while concurrently lowering the vacuum energy level ( $E_{\text{vacuum}}$ ). This modification resulted in a reduction of the work function from 5.43 eV in pristine ZnO to 4.93 eV in Co substituted Zn ( $\text{Co}_{\text{SA}/\text{Zn}}\text{-ZnO}$ ) and further down to 4.24 eV in Co substituted Zn and O ( $\text{Co}_{\text{SA}/\text{Zn},\text{O}}\text{-ZnO}$ ). These adjustments were favorable for enhancing electron transfer processes in the material. Pristine ZnO displayed non-spin polarization, and its density of states (DOS) exhibited symmetry. However, introducing a single Co atom onto the ZnO surface disrupted this symmetry, particularly near the Fermi energy level (Supplementary Fig. 68). This disruption indicated that the spin polarization within the material was predominantly associated with the Co sites. A further analysis (Fig. 4b) reveals that the spin-charge was primarily localized at the Co site. This finding implies that the spin polarization of neighboring O atoms was enhanced through  $d$ - $p$  orbital hybridization. Such spin polarization was crucial, as it could strengthen reactant adsorption and electron transfer, significantly improving the catalytic performance of the material.

Given that the projected DOS (PDOS) of the  $3d$  orbitals of transition metals was highly localized near the Fermi energy level and crucial for catalytic reactions, we further investigated the PDOS of the  $3d$  orbital of the surface-active sites (Fig. 4d-f). After anchoring Co atoms into ZnO, the  $d$ -band of the surface Co-Zn atom pair showed a significantly polarized PDOS near the Fermi energy level, and the center of its  $d$ -band was significantly shifted upward. Regarding the spin polarization, the  $d$ -band centers for  $\alpha$ -spin ( $E_{d\alpha}$ ) and  $\beta$ -spin ( $E_{d\beta}$ ) were shifted upward to -4.33 eV and -3.11 eV, respectively, in the  $\text{Co}_{\text{SA}/\text{Zn}}\text{-ZnO}$  configuration. In the  $\text{Co}_{\text{SA}/\text{Zn},\text{O}}\text{-ZnO}$  structure, these  $d$ -band centers were elevated to -4.43 eV ( $\alpha$ -spin) and -3.32 eV ( $\beta$ -spin). According to the  $d$ -band center theory<sup>46</sup>, an upward shift in the  $d$ -band center enhanced the adsorption of PMS, consequently facilitating its activation. To illuminate the distinctive contributions of Co and Zn, a comprehensive analysis of the  $d$ -band centers for Co and Zn was conducted individually (Fig. 4h). For non-spin-polarized ZnO, both Zn sites involved in PMS adsorption exhibited identical  $E_{d\alpha}$  and  $E_{d\beta}$  values, situated around -5.4 eV. In the case of  $\text{Co}_{\text{SA}/\text{Zn}}\text{-ZnO}$ , the inclusion of doped Co atoms led to a slight downward shift in the  $d$ -band center of the adjacent Zn. Specifically, the Co atoms exhibited  $E_{d\alpha}$  and  $E_{d\beta}$  values at -2.66 eV and -0.08 eV, respectively, indicative of the spin-polarized nature of their  $d$ -band PDOS. This configuration fostered a synergistic interaction with the frontier orbitals of PMS, enhancing the overall catalytic efficiency. A similar phenomenon was observed for  $\text{Co}_{\text{SA}/\text{Zn},\text{O}}\text{-ZnO}$ .

We further investigated the adsorption energy and bader-charge transfer when PMS adsorbed on the catalyst surface (Fig. 4g and Supplementary Figs. 69, 70). Benefiting from the upward shift of the  $d$ -band center and decreased work function, the introduction of Co into the ZnO significantly heightened the adsorption energy of PMS on both  $\text{Co}_{\text{SA}/\text{Zn},\text{O}}\text{-ZnO}$  and  $\text{Co}_{\text{SA}/\text{Zn}}\text{-ZnO}$  catalysts, elevating it from -2.75 eV to -3.63 eV. This increase was accompanied by an enhanced charge transfer, from 0.74 e to 0.81 e. Despite  $\text{Co}_{\text{SA}/\text{Zn},\text{O}}\text{-ZnO}$  having a marginally lower  $d$ -band center compared to  $\text{Co}_{\text{SA}/\text{Zn}}\text{-ZnO}$ , its PMS adsorption energy was more substantial. This discrepancy was likely attributable to van der Waals interactions between PMS and the

exposed Zn sites on  $\text{Co}_{\text{SA}/\text{Zn},\text{O}}\text{-ZnO}$ . To comprehend the specific contributions of Zn and Co sites to PMS adsorption, we employed the projected crystal orbital Hamilton population (PCOHP) and integrated COHP (ICOHP) analysis<sup>47,48</sup> (Fig. 4i, j). In pure ZnO, both  $\text{Zn}_1\text{-O}_1$  and  $\text{Zn}_2\text{-O}_2$  atom pairs (Supplementary Fig. 71) appeared to contribute equally to PMS adsorption. Furthermore, for both  $\alpha$ -spin and  $\beta$ -spin, the contributions were nearly identical, with similar electron distributions in the antibonding regions. For  $\text{Co}_{\text{SA}/\text{Zn},\text{O}}\text{-ZnO}$  system, a pronounced bonding contribution was observed from  $\text{Co}_1\text{-O}_2$  (Supplementary Fig. 71), significantly stronger than that from the  $\text{Zn}_1\text{-O}_1$  pair (ICOHP values: -0.797 vs. -0.547). Notably, the  $\beta$ -spin's higher  $d$ -band center in  $\text{Co}_{\text{SA}/\text{Zn},\text{O}}\text{-ZnO}$  lifted the antibonding orbitals and decreased the electron occupancy in these regions, leading to a lower ICOHP value for the  $\text{Co}_1\text{-O}_2$  bond in  $\beta$ -spin (-1.019) compared to  $\alpha$ -spin (-0.520). These observations reveal two crucial aspects: (1) The augmented bonding contribution primarily originates from the  $\beta$ -spin electrons of Co, and (2) Strong PMS adsorption on  $\text{Co}_{\text{SA}/\text{Zn},\text{O}}\text{-ZnO}$  was facilitated by both the spin polarization and the elevated  $d$ -band center of Co.

To further understand the catalytic process from a thermodynamic perspective, we calculated the Gibbs free energy of the catalytic reaction. The  $\text{Co}_{\text{SA}/\text{Zn},\text{O}}\text{-ZnO}$  catalyst demonstrated significantly lower dissociation energy for the O-O bond in PMS (-3.12 eV, Fig. 4k) compared to ZnO (0.20 eV), aligning with observed reaction kinetics. This result implies that  $\text{Co}_{\text{SA}/\text{Zn},\text{O}}\text{-ZnO}$  is more adept at activating PMS to generate reactive species. Moreover, when considering the selective generation of radicals following bond dissociation, both  $\text{Co}_{\text{SA}/\text{Zn},\text{O}}\text{-ZnO}$  and ZnO showed a preference, indicated by lower  $\Delta G$ , for the formation of  $\text{SO}_4^{\cdot-}$  over  $\cdot\text{OH}$  (Fig. 4l, m and Supplementary Figs. 72, 73), suggesting a bias towards highly-oxidative  $\text{SO}_4^{\cdot-}$  radicals formation in the catalytic reaction.

The above theoretical calculations offer deep insights into the reaction mechanisms underlying the "island-sea" Co SAC-activated PMS system. This meticulous approach has not only elucidated the intricate interplay between the catalyst's structural attributes and catalytic behaviors, but also provided a framework for optimizing the catalyst model to align accurately with experimental designs.

### Pilot-scale experiments and full-scale toxicity assessment of the $\text{Co}_{\text{SA}/\text{Zn},\text{O}}\text{-ZnO}/\text{PMS}$

To evaluate the practical applicability of the  $\text{Co}_{\text{SA}/\text{Zn},\text{O}}\text{-ZnO}/\text{PMS}$  system, a continuous flow reactor was constructed for the sustained degradation of pollutants (Fig. 5a, h). The  $\text{Co}_{\text{SA}/\text{Zn},\text{O}}\text{-ZnO}$  membrane, fabricated using a vacuum-assisted technique, exhibited notable flexibility and adhesion, ensuring catalyst integrity throughout the reaction process (Fig. 5b-d). The water contact angle (WCA) measurements indicated enhanced hydrophilicity of the  $\text{Co}_{\text{SA}/\text{Zn},\text{O}}\text{-ZnO}$  membrane (23.2°) compared to that of the standard MCE membrane (79.5°) (Fig. 5e-g). The increased hydrophilicity is advantageous for lowering water transport resistance and mitigating membrane fouling<sup>49</sup>. To visually demonstrate the catalytic system's efficacy, RhB was chosen as a model pollutant. The effluent was colorless after filtration through the  $\text{Co}_{\text{SA}/\text{Zn},\text{O}}\text{-ZnO}/\text{MCE}$  membrane, indicating nearly complete removal of RhB after 12 h continuous operation (Fig. 5i and Supplementary Fig. 74). Moreover, the system consistently maintained a high removal rate of approximately 95% for SMX over a 12 h period (Supplementary Fig. 75).

Primarily, the constructed reaction reactor exhibited remarkable efficacy in treating authentic coking wastewater. Firstly, evident decolorization of coking wastewater treated with the  $\text{Co}_{\text{SA}/\text{Zn},\text{O}}\text{-ZnO}/\text{MCE}$  catalytic membrane was observed (Fig. 5j and Supplementary Fig. 76). Secondly, the TOC removal of coking wastewater reached ~80% within 1 h of the reaction. Even after 12 h of continuous operation, the TOC removal remained at ~50% (Fig. 5j). To verify the feasibility of the  $\text{Co}_{\text{SA}/\text{Zn},\text{O}}\text{-ZnO}/\text{PMS}$  system for practical application, pilot-scale experiments were conducted to treat antibiotic wastewater and coking wastewater<sup>50</sup>. As shown in Fig. 5l, the photographs depict the entire

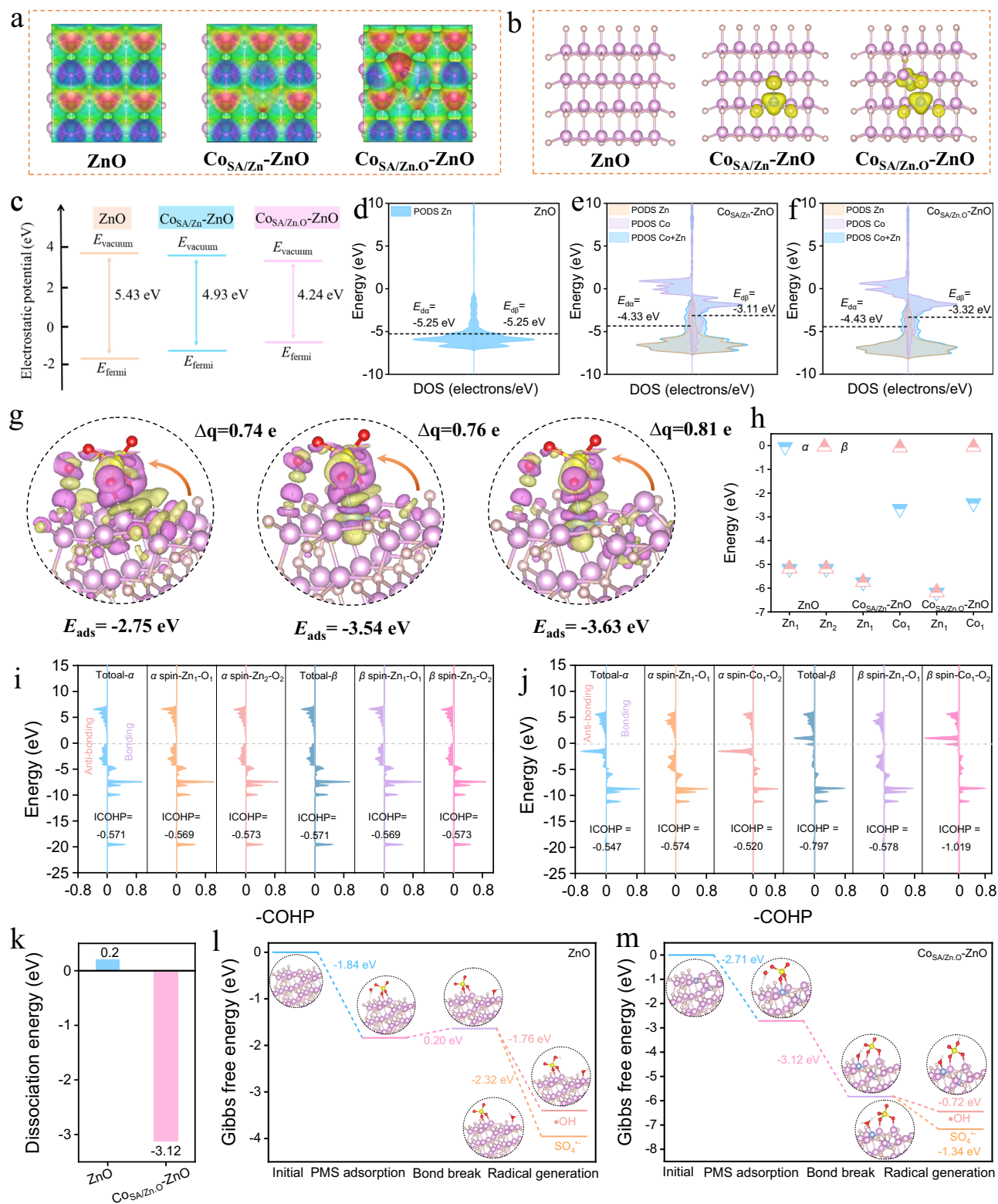


**Fig. 4 | DFT calculations for elucidating the underlying mechanisms.**

**a** Electrostatic potential of the material surface (blue means negatively charged, red means positively charged). **b** Spin charge density (the yellow area represents the spin charge). **c** Work function of ZnO, CoSA/Zn-ZnO, and CoSA/ZnO-ZnO. **d-f** pDOS of ZnO, CoSA/Zn-ZnO and CoSA/ZnO-ZnO. **g** PMS adsorption energy, differential charge density, and Bader charge analysis of ZnO, CoSA/Zn-ZnO, and CoSA/ZnO-ZnO,

respectively (The pink and yellow areas represent regions of electron gain and loss, respectively). **h** Spin-polarized *d*-band centers of ZnO, CoSA/Zn-ZnO, and CoSA/ZnO-ZnO. **i** COHP diagram for PMS adsorption of ZnO and CoSA/ZnO-ZnO. **k** Bond dissociation energy of O-O bond in PMS on ZnO and CoSA/ZnO-ZnO. **l** Calculated Gibbs free energy for PMS activation on ZnO and CoSA/ZnO-ZnO.

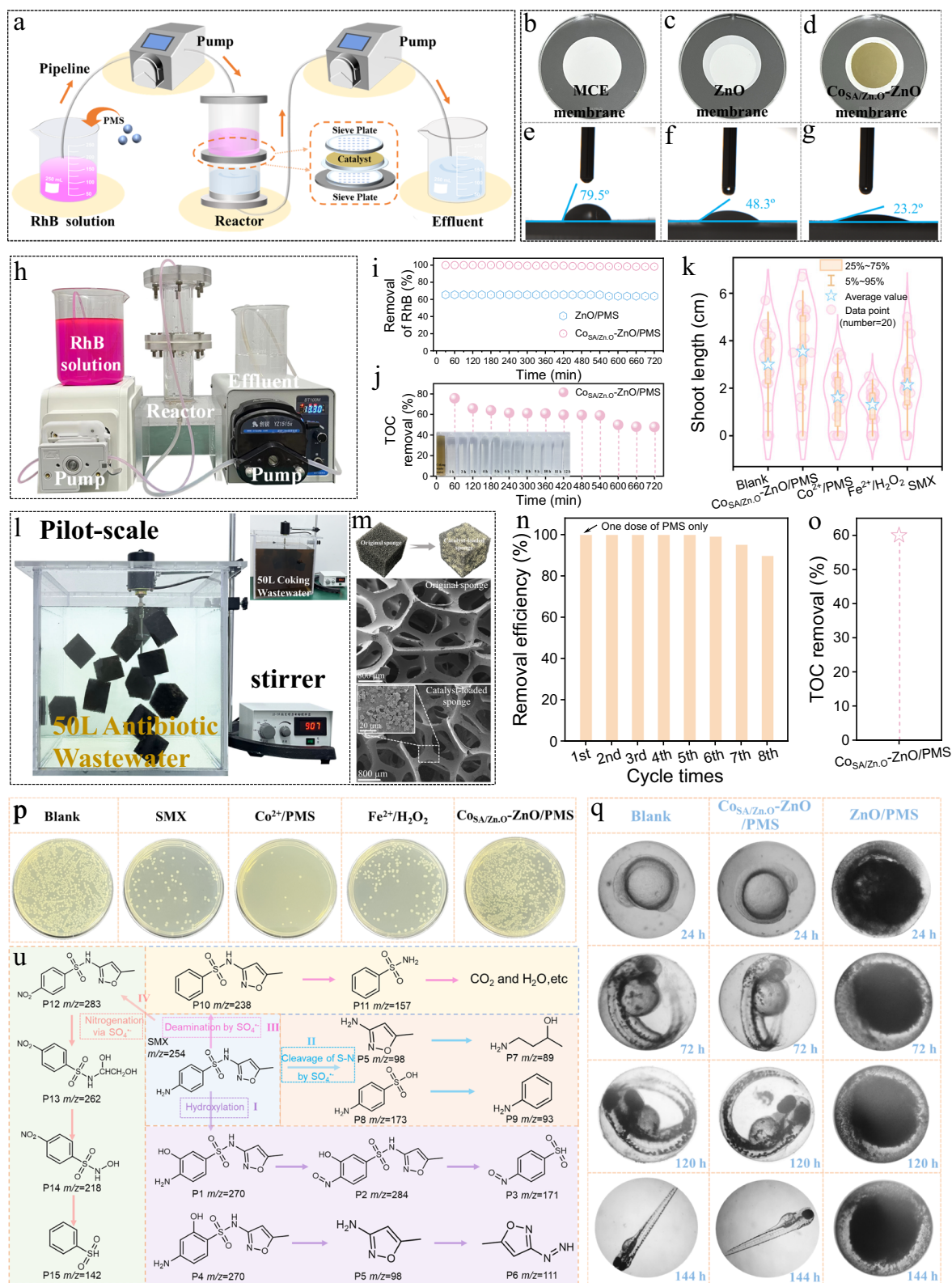


**Fig. 5 | Pilot-scale experiment and comprehensive toxicity evaluation of the  $\text{Co}_{\text{SA}}/\text{ZnO-ZnO}/\text{PMS}$  system.** **a** Schematic diagram of continuous flow reactor. Photographs of **(b)** pure MCE membrane, **(c)** ZnO/MCE, and **(d)**  $\text{Co}_{\text{SA}}/\text{ZnO-ZnO}/\text{MCE}$  membranes. Contact angles of **(e)** MCE membrane, **(f)** ZnO/MCE, and **(g)**  $\text{Co}_{\text{SA}}/\text{ZnO-ZnO}/\text{MCE}$  membranes with water. **h** Photograph of continuous flow reactor. **i** Continuous removal of RhB in the ZnO/PMS and  $\text{Co}_{\text{SA}}/\text{ZnO-ZnO}/\text{PMS}$  systems. **j** TOC removal efficiency of coking wastewater treated by continuous flow reactor (inset: Color change of coking wastewater). **k** Violin plots of wheat shoot length distribution in various systems. **l** Pilot-scale experiment diagram for treating 50 L of

antibiotic wastewater (inset: Pilot-scale experiment diagram for treating 50 L of coking wastewater). **m** Comparison of the appearance and SEM images of the pristine sponge and the catalyst-loaded sponge (inset: enlarged view of catalyst morphology on sponge skeleton). **n** Cyclic degradation effect of treating 50 L of antibiotic wastewater. **o** TOC removal efficiency for treating 50 L of coking wastewater. **p** Photographs of *E. coli* colonies cultured with solution treated with different systems. **q** Growth of zebrafish cultured in the solution treated with ZnO/PMS and  $\text{Co}_{\text{SA}}/\text{ZnO-ZnO}/\text{PMS}$  systems. **u** Analysis of possible degradation pathways of SMX in the  $\text{Co}_{\text{SA}}/\text{ZnO-ZnO}/\text{PMS}$  system.

degradation setup used for this experiment. Specifically, 50 L of antibiotic and coking wastewater were added into a 40 cm × 40 cm × 38 cm transparent Plexiglas tank and stirred by a mechanical stirrer. The catalysts in this system could be scaled up for gram-scale preparation, demonstrating high potential for practical applications (Supplementary Fig. 77). A polyurethane sponge was selected as the carrier for immobilizing the catalyst. SEM images and mapping results revealed that the sponge substrate had a dense skeletal structure with pores, and the  $\text{Co}_{\text{SA}/\text{Zn}_2\text{O}}\text{-ZnO}$  catalysts were evenly distributed on its surface (Fig. 5m and Supplementary Fig. 78). The ability of the sponge to suspend in the wastewater ensured adequate interaction between the catalyst, PMS, and contaminants. Additionally, the sponge facilitated the recovery and reuse of the catalyst after degradation, thus minimizing costs and reducing the risk of secondary environmental contamination. The  $\text{Co}_{\text{SA}/\text{Zn}_2\text{O}}\text{-ZnO/PMS}$  system effectively treated both antibiotic and actual coking wastewater. With only a single dosing of PMS, the system maintained excellent treatment results over time, achieving antibiotic removal rates approaching 90% after eight cycles (Fig. 5n). Furthermore, the color of the coking wastewater was significantly lightened, and the mineralization reached 60% after 8 h of continuous treatment (Fig. 5o and Supplementary Fig. 79). These findings demonstrated the exceptional practical utility of the devised system. Thus, these results highlight the  $\text{Co}_{\text{SA}/\text{Zn}_2\text{O}}\text{-ZnO/PMS}$  system's capability for long-term, efficient pollutant degradation, demonstrating its great potential for real-world applications in wastewater treatment.

Moreover, DFT calculations were used to predict the reactive sites on SMX molecules<sup>51,52</sup>. First, orbital-weighted Fukui functions  $f^0$  and  $f^-$  were applied to analyze the SMX structure, revealing that the most susceptible site for radical ( $\text{SO}_4^{\cdot-}$ ) (Supplementary Fig. 80a and Supplementary Table 21) attack was the nitrogen atom at position 17(N), which displayed the highest  $f^0$  value<sup>53</sup>. Additionally, molecular electrostatic potential analysis (Supplementary Fig. 80a) indicated that the aniline moiety of SMX was highly positively charged, suggesting its potential as a reactive site for  $\text{ROS}^{\cdot}$ . The highest occupied molecular orbital (HOMO) (Supplementary Fig. 80b) of SMX was predominantly located on the benzene ring, indicating its vulnerability to attack. Consequently, 17(N) and 4(C) were in the most vulnerable position and were susceptible to cleavage by attack.

The proposed degradation pathways of SMX (Fig. 5u) in the  $\text{Co}_{\text{SA}/\text{Zn}_2\text{O}}\text{-ZnO/PMS}$  system were deduced by integrating liquid chromatography-mass spectrometry results (Supplementary Fig. 81 and Supplementary Table 22) with DFT findings. Pathway I involved the initial transformation of SMX to products P1 and P4 ( $m/z = 270$ ), followed by the oxidation of the  $-\text{NH}_2$  group in P1 to yield P2 ( $m/z = 284$ ) and subsequent S-N bond cleavage leading to P3 ( $m/z = 171$ )<sup>7</sup>. Then, the S-N bond in P4 was broken to form P5 ( $m/z = 98$ ), which then underwent coupling to form the oxazole ring (P6,  $m/z = 111$ )<sup>55</sup>. In pathway II,  $\text{SO}_4^{\cdot-}$  attacked SMX, breaking the S-N bond to yield P-8 ( $m/z = 173$ ) and P-5 ( $m/z = 98$ ), which were then oxidized to P7 ( $m/z = 89$ ) and P9 ( $m/z = 93$ ), respectively<sup>56</sup>. Pathway III involved deamination and C-N bond breakage due to  $\text{SO}_4^{\cdot-}$  attack, resulting in P10 ( $m/z = 238$ ) and P11 ( $m/z = 157$ )<sup>57</sup>. Pathway IV initiated with oxidation of the  $-\text{NH}_2$  group on the SMX benzene ring to form P12 ( $m/z = 283$ )<sup>58</sup>, followed by the breaking of the oxazole ring and double bond to generate P13 ( $m/z = 262$ ), which underwent further oxidative transformation to P14 ( $m/z = 218$ ) and P15 ( $m/z = 142$ )<sup>55</sup>. Ultimately, these intermediates were further mineralized to water and carbon dioxide through additional oxidation.

To ascertain the real-world applicability of the catalytic systems, the toxicity of SMX and its intermediates was initially predicted using the Ecological Structure-Activity Relationships (ECOSAR) system and the Toxicity Estimation Software Tool (T.E.S.T.) system (Supplementary Fig. 82 and Supplementary Table 23)<sup>59</sup>. Following this, the toxicity of the  $\text{Co}_{\text{SA}/\text{Zn}_2\text{O}}\text{-ZnO/PMS}$ -treated solution was comprehensively assessed through a comparative analysis of its effects on

microorganisms, plants, and animals. The study revealed that solutions treated with conventional Fenton ( $\text{Fe}^{2+}/\text{H}_2\text{O}_2$ ) and Fenton-like ( $\text{Co}^{2+}/\text{PMS}$ ) systems exhibited higher toxicity and a reduced density of *Escherichia coli* (*E. coli*) (Fig. 5p), primarily due to the presence of toxic cobalt ions and iron sludge, which hindered *E. coli* growth. In contrast, the colony density of *E. coli* in the solution treated with  $\text{Co}_{\text{SA}/\text{Zn}_2\text{O}}\text{-ZnO/PMS}$  was similar to that of the control group (Fig. 5p), indicating low to negligible toxicity of the degradation products. This trend was further corroborated by wheat growth experiments, where the germination rate and shoot length of wheat grown in the  $\text{Co}_{\text{SA}/\text{Zn}_2\text{O}}\text{-ZnO/PMS}$ -treated solution even exceeded those of the control (Fig. 5k and Supplementary Figs. 83, 84). This enhancement was attributed to the role of trace Zn ions precipitated by the system, acting as a zinc fertilizer to promote wheat growth. These results affirm that the wastewater treated by the  $\text{Co}_{\text{SA}/\text{Zn}_2\text{O}}\text{-ZnO/PMS}$  system was non-toxic and safe, making it suitable for crop irrigation and cultivation (Supplementary Fig. 85). Additionally, zebrafish growth experiments supported these findings (Fig. 5q). During a 144-h observation period, no abnormalities or fatalities were noted in zebrafish cultured in both the  $\text{Co}_{\text{SA}/\text{Zn}_2\text{O}}\text{-ZnO/PMS}$  treated water and the control group, underscoring the effective detoxification capability of the  $\text{Co}_{\text{SA}/\text{Zn}_2\text{O}}\text{-ZnO/PMS}$  system. In stark contrast, zebrafish in the ZnO group exhibited early mortality, paralleling results from the SMX control group (Supplementary Fig. 86). These results collectively indicate that the  $\text{Co}_{\text{SA}/\text{Zn}_2\text{O}}\text{-ZnO/PMS}$  system was not only effective in degrading organic pollutants, but also ensured the production of non-toxic byproducts. The multifunctional integrated system, which combined efficient pollutant degradation, detoxification, and crop irrigation, demonstrates the significant practical potential for real-world water purification applications.

## Discussion

In this study, we engineered a functionalized single-atom nano-island catalyst,  $\text{Co}_{\text{SA}/\text{Zn}_2\text{O}}\text{-ZnO}$ , designed to enhance both activity and stability in Fenton-like reactions. This structural design leveraged the synergistic interaction between the “island” (atomically dispersed Co atoms on ZnO nanoparticles) and the “sea” (the ZnO substrate), each fulfilling distinct roles in activating PMS. The “island” ensured the confinement and stabilization of Co atoms, while the “sea” maintained a neutral reaction microenvironment. The  $\text{Co}_{\text{SA}/\text{Zn}_2\text{O}}\text{-ZnO/PMS}$  system exhibited a great performance in the selective generation of highly oxidative  $\text{SO}_4^{\cdot-}$ , achieving complete degradation of various pollutants at a self-stabilizing pH system. Remarkably, a degradation rate constant ( $k$ -value) of  $98.2 \text{ min}^{-1} \text{ M}^{-1}$  was observed for antibiotic SMX, outperforming previously reported catalysts.

Additionally,  $\text{Co}_{\text{SA}/\text{Zn}_2\text{O}}\text{-ZnO}$  demonstrated strong resilience against varied environmental factors and a wide array of organic compounds. It exhibited ultra-low active site leaching and remarkable cyclic stability. Theoretical computations reveal that the integration of monoatomic Co sites altered the symmetry of the electronic structure and elevated the  $d$ -band center. These changes significantly enhanced PMS adsorption and facilitated the generation of  $\text{SO}_4^{\cdot-}$  radicals. Toxicity assessments using comprehensive zebrafish, wheat, and *E. coli* experiments confirmed the non-toxic nature of degradation products. Moreover, the swift decolorization and substantial mineralization of coking wastewater over extended continuous flow durations (12 h) revalidated the distinctive design of the reaction system and demonstrated its promising practical applicability. This approach effectively resolves the longstanding challenge of balancing catalytic activity and stability, offering fresh perspectives and strategies for the efficient development of advanced “island-sea” or other functionalized SACs in water decontamination and high-value conversion reactions.

## Methods

### Chemicals and reagents

Detailed information is provided in the Supplementary Information.

## Construction of nano-island Co SACs

- (1) Preparation of  $\text{Co}_{\text{SA}/\text{Zn}_2\text{O}}\text{-ZnO}$ : initially,  $\text{Zn}(\text{CH}_3\text{COO})_2$  (0.734 g, 4 mmol) and  $\text{Co}(\text{CH}_3\text{COO})_2 \cdot 4\text{H}_2\text{O}$  (0.0498 g, 0.2 mmol) were dissolved in 40 mL of ethanol ( $\text{C}_2\text{H}_5\text{OH}$ ). This mixture was stirred continuously for 1 h. Subsequently, 40 mL of a 0.1 M KOH solution was added gradually, with continued stirring for an additional 6 h, resulting in a viscous precursor solution. This precursor was then transferred to a Teflon-lined autoclave and subjected to a temperature of 150 °C for 20 h. Post-synthesis, the resultant material was thoroughly washed thrice using deionized water and  $\text{C}_2\text{H}_5\text{OH}$  and subsequently dried at 60 °C over 12 h. Ultimately, a 0.198 g sample can be obtained. The synthesized sample was denoted as 5%  $\text{Co}_{\text{SA}/\text{Zn}_2\text{O}}\text{-ZnO}$ , where 5% signified the molar ratio of Co to Zn in the composite. To obtain catalysts with varying Co concentrations, similar procedures were employed with adjusted quantities of  $\text{Co}(\text{CH}_3\text{COO})_2 \cdot 4\text{H}_2\text{O}$ , yielding 1%  $\text{Co}_{\text{SA}/\text{Zn}_2\text{O}}\text{-ZnO}$  and 10%  $\text{Co}_{\text{SA}/\text{Zn}_2\text{O}}\text{-ZnO}$  variants. Unless explicitly stated otherwise in this thesis, the term  $\text{Co}_{\text{SA}/\text{Zn}_2\text{O}}\text{-ZnO}$  refers to the 5%  $\text{Co}_{\text{SA}/\text{Zn}_2\text{O}}\text{-ZnO}$  variant.
- (2) Preparation of other transition metal-based SACs: the synthesis procedure for alternative metal-doped ZnO catalysts paralleled that of  $\text{Co}_{\text{SA}/\text{Zn}_2\text{O}}\text{-ZnO}$ , with the primary variation being using distinct metal precursors.
- (3) Preparation of ZnO: the preparation of pristine ZnO was similar to that of  $\text{Co}_{\text{SA}/\text{Zn}_2\text{O}}\text{-ZnO}$ , with the primary distinction being the exclusion of  $\text{Co}(\text{CH}_3\text{COO})_2 \cdot 4\text{H}_2\text{O}$  from the precursor mixture. Ultimately, a 0.196 g sample can be obtained.

## Characterizations

XANES analyses at the Co K-edge were performed using a commercial XAFS instrument (easyXAFS300, easy XAFS LLC, Renton, WA), designed on the principles of Rowland circle geometries. For high-precision measurements, this setup included spherically bent crystal analyzers and a silicon drift detector (AXAS-MI, KETEK GmbH, Germany). High-angle annular dark-field scanning transmission electron microscopy (HAADF-STEM) imaging was executed with a high-resolution transmission electron microscope (FEI, Titan Cubed Themis G2 300; JEM-ARM300F), providing insights into the catalyst's morphological and structural attributes. Additional characterizations of the catalysts, along with relevant theoretical calculations, are described in the Supplementary Information.

## Catalytic performance evaluation

Degradation assays were conducted in a 50 mL aqueous suspension, comprising  $0.1 \text{ g L}^{-1}$  of the synthesized catalyst, 0.5 mM PMS, and  $10 \text{ mg L}^{-1}$  SMX. All batch experiments were carried out within the same temperature range. To ensure equilibrium between adsorption and desorption, the catalyst and SMX were pre-mixed and agitated for 15 min before the introduction of PMS. Subsequent to PMS addition, 1 mL aliquot was extracted from the suspension bi-minutely. These aliquots were promptly quenched with 0.1 mL of 80 mM sodium thiosulfate solution to halt the catalytic reaction. Post-quenching, the samples underwent centrifugation at  $18,630 \times g$  for 20 min to facilitate the separation of suspended particulates. The supernatant was then subjected to quantitative analysis of residual SMX concentration using high-performance liquid chromatography (HPLC, 1260 Infinity, Agilent Inc., USA). For the extended continuous flow experiments involving coking wastewater and laboratory water distribution, we assembled a reaction system equipped with a tall column support (Supplementary Fig. 76).

## Details of density functional theory (DFT) calculations

We performed DFT calculations using the generalized gradient approximation (GGA) framework, specifically the Perdew-Burke-Ernzerhof (PBE) formulation. For the optimization of geometry, a

Brillouin zone of  $2^*2^*1$  k-points was utilized<sup>60</sup>. Valence electrons were represented using a plane-wave basis set with a kinetic energy cutoff of 400 eV. Partial occupancies of the Kohn-Sham orbitals were incorporated using the Gaussian smearing method, set at a width of 0.05 eV. Self-consistency in the electronic energy calculations was ensured by adopting a convergence criterion where the energy change was smaller than  $10^{-5}$  eV. Additionally, geometry optimization was considered convergent if the energy change was less than 0.02 eV per Ångström ( $\text{eV \AA}^{-1}$ ). To avoid artificial interactions between periodic images, a vacuum layer of 15 Å thickness was typically employed. For treating weak interactions, the DFT + D3 method was utilized, incorporating Grimme's empirical dispersion correction.

## Reporting summary

Further information on research design is available in the Nature Portfolio Reporting Summary linked to this article.

## Data availability

The data supporting the findings of the study are included in the main text and Supplementary Information files. Raw data can be obtained from the corresponding authors upon request. Source data are provided with this paper.

## References

1. Meng, Y. et al. Nanoconfinement steers nonradical pathway transition in single atom Fenton-like catalysis for improving oxidant utilization. *Nat. Commun.* **15**, 5314 (2024).
2. Zhang, T. et al. Superexchange-induced Pt-O-Ti<sup>3+</sup> site on single photocatalyst for efficient H<sub>2</sub> production with organics degradation in wastewater. *Proc. Natl Acad. Sci. USA* **120**, e2302873120 (2023).
3. Liu, J. Y. et al. Direct electron transfer-driven nontoxic oligomeric deposition of sulfonamide antibiotics onto carbon materials for in situ water remediation. *Environ. Sci. Technol.* **58**, 12155–12166 (2024).
4. Zhang, Z. Q. et al. Modified-pollen confined hybrid system: a promising union for visible-light-driven photocatalytic antibiotic degradation. *Appl. Catal. B Environ.* **330**, 122621 (2023).
5. Wu, Z. et al. Facile tuning the first-shell coordination micro-environment in iron single-atom for Fenton-like chemistry toward highly efficient wastewater purification. *Environ. Sci. Technol.* **57**, 14046–14057 (2023).
6. Li, X. et al. Single cobalt atoms anchored on porous N-doped graphene with dual reaction sites for efficient Fenton-like catalysis. *J. Am. Chem. Soc.* **140**, 12469–12475 (2018).
7. Zhou, Q. et al. Generating dual-active species by triple-atom sites through peroxymonosulfate activation for treating micropollutants in complex water. *Proc. Natl Acad. Sci. USA* **120**, e2300085120 (2023).
8. Huang, B. et al. Modulating electronic structure engineering of atomically dispersed cobalt catalyst in Fenton-like reaction for efficient degradation of organic pollutants. *Environ. Sci. Technol.* **57**, 14071–14081 (2023).
9. Mo, F. et al. The optimized Fenton-like activity of Fe single-atom sites by Fe atomic clusters-mediated electronic configuration modulation. *Proc. Natl Acad. Sci. USA* **120**, e2300281120 (2023).
10. Deng, J. et al. Advances of carbon nitride based atomically dispersed catalysts from single-atom to dual-atom in advanced oxidation process applications. *Coord. Chem. Rev.* **505**, 215693 (2024).
11. Zeng, Y. et al. Mediated peroxymonosulfate activation at the single atom Fe-N<sub>3</sub>O<sub>1</sub> sites: synergistic degradation of antibiotics by two non-radical pathways. *Small* **20**, e2311552 (2024).
12. Wang, Z. et al. Cobalt single atoms anchored on oxygen-doped tubular carbon nitride for efficient peroxymonosulfate activation: simultaneous coordination structure and morphology modulation. *Angew. Chem. Int. Ed.* **61**, 202202338 (2022).

13. Shang, Y., Xu, X., Gao, B., Wang, S. & Duan, X. Single-atom catalysis in advanced oxidation processes for environmental remediation. *Chem. Soc. Rev.* **50**, 5281–5322 (2021).
14. Chen, F. et al. Single-atom iron anchored tubular g-C<sub>3</sub>N<sub>4</sub> catalysts for ultrafast Fenton-like reaction: roles of high-valency iron-oxo species and organic radicals. *Adv. Mater.* **34**, 2202891 (2022).
15. Li, Z., Li, B. & Li, Q. Single-atom nano-islands (SANIs): a robust atomic-nano system for versatile heterogeneous catalysis applications. *Adv. Mater.* **35**, 2211103 (2023).
16. Denisov, N. et al. Light-induced agglomeration of single-atom platinum in photocatalysis. *Adv. Mater.* **35**, 2206569 (2023).
17. Xiong, H., Datye, A. K. & Wang, Y. Thermally stable single-atom heterogeneous catalysts. *Adv. Mater.* **33**, 2004319 (2021).
18. Li, X. et al. Functional CeO<sub>x</sub> nanoglues for robust atomically dispersed catalysts. *Nature* **611**, 284–288 (2022).
19. Liu, X. et al. Directional growth and density modulation of single-atom platinum for efficient electrocatalytic hydrogen evolution. *Angew. Chem. Int. Ed.* **63**, e202406650 (2024).
20. Sun, P. et al. Constructing amorphous-crystalline interfacial bifunctional site island-sea synergy by morphology engineering boosts alkaline seawater hydrogen evolution. *Adv. Sci.* **11**, 2309927 (2024).
21. Bao, Y., Liu, W., Cao, J., Zhang, J. & Xing, M. Self-neutralized conditions constructed by amphoteric zinc in cobalt-induced peroxy-monosulfate activation for sustainable degradation of organic pollutants. *ACS EST Eng.* **3**, 1956–1965 (2023).
22. Tian, B. et al. Doping engineering to modulate lattice and electronic structure for enhanced piezocatalytic therapy and ferroptosis. *Adv. Mater.* **35**, 2304262 (2023).
23. Wen, Y. et al. Two birds with one stone: cobalt-doping induces to enhanced piezoelectric property and persulfate activation ability of ZnO nanorods for efficient water purification. *Nano Energy* **107**, 108173 (2023).
24. Wu, X. L. et al. Directional and ultrafast charge transfer in oxygen-vacancy-rich ZnO@single-atom cobalt core-shell junction for photo-Fenton-like reaction. *Angew. Chem. Int. Ed.* **62**, e202305639 (2023).
25. Sun, T. et al. Single-atomic cobalt sites embedded in hierarchically ordered porous nitrogen-doped carbon as a superior bifunctional electrocatalyst. *Proc. Natl Acad. Sci. USA* **115**, 12692–12697 (2018).
26. Qian, M. et al. Modulation of charge trapping by island-like single-atom cobalt catalyst for enhanced photo-Fenton-like reaction. *Adv. Funct. Mater.* **33**, 2208688 (2023).
27. Zheng, X. et al. Ru-Co pair sites catalyst boosts the energetics for the oxygen evolution reaction. *Angew. Chem. Int. Ed.* **61**, e202205946 (2022).
28. Song, J. et al. Asymmetrically coordinated CoB<sub>1</sub>N<sub>3</sub> moieties for selective generation of high-valence Co-Oxo species via coupled electron-proton transfer in Fenton-like reactions. *Adv. Mater.* **35**, 2209552 (2023).
29. Li, X. et al. CoN<sub>1</sub>O<sub>2</sub> single-atom catalyst for efficient peroxy-monosulfate activation and selective cobalt<sup>(IV)</sup>=O generation. *Angew. Chem. Int. Ed.* **62**, 202303267 (2023).
30. Mi, X. et al. Almost 100 % peroxy-monosulfate conversion to singlet oxygen on single-atom CoN<sub>2+2</sub> sites. *Angew. Chem. Int. Ed.* **60**, 4588–4593 (2021).
31. Bao, Y. et al. Generating high-valent iron-oxo Fe<sup>IV</sup>=O complexes in neutral microenvironments through peroxy-monosulfate activation by Zn-Fe layered double hydroxides. *Angew. Chem. Int. Ed.* **61**, 202209542 (2022).
32. Wei, S. et al. Self-carbon-thermal-reduction strategy for boosting the Fenton-like activity of single Fe-N<sub>4</sub> sites by carbon-defect engineering. *Nat. Commun.* **14**, 7549 (2023).
33. Zhang, D. et al. Dynamic active-site induced by host-guest interactions boost the Fenton-like reaction for organic wastewater treatment. *Nat. Commun.* **14**, 3538 (2023).
34. Xu, J. et al. Unveiling enhanced electron-mediated peroxy-monosulfate activation for degradation of emerging organic pollutants. *Appl. Catal. B Environ.* **341**, 123356 (2024).
35. Chen, F. et al. Embedding electronic perpetual motion into single-atom catalysts for persistent Fenton-like reactions. *Proc. Natl Acad. Sci. USA* **121**, 2314396121 (2024).
36. Shao, H. et al. Naproxen as a turn-on chemiluminescent probe for real-time quantification of sulfate radicals. *Environ. Sci. Technol.* **57**, 8818–8827 (2023).
37. Su, L. et al. Mn-enhanced cobalt silicate-activated peroxy-monosulfate for tetracycline degradation: inheriting merit and offsetting deficiency of oxygen vacancies. *ACS EST Eng.* **3**, 1614–1625 (2023).
38. Bai, C. W. et al. Circumventing bottlenecks in H<sub>2</sub>O<sub>2</sub> photosynthesis over carbon nitride with iodine redox chemistry and electric field effects. *Nat. Commun.* **15**, 4718 (2024).
39. Li, F. et al. Efficient photo-Fenton reaction for tetracycline and antibiotic resistant bacteria removal using hollow Fe-doped In<sub>2</sub>O<sub>3</sub> nanotubes: from theoretical research to practical application. *Water Res.* **240**, 120088 (2023).
40. Huang, B. et al. Coupled surface-confinement effect and pore engineering in a single-Fe-atom catalyst for ultrafast Fenton-like reaction with high-valent iron-oxo complex oxidation. *Environ. Sci. Technol.* **57**, 15667–15679 (2023).
41. Xiao, Y. et al. Constructing zinc single-atom catalysts for the direct electron-transfer mechanism in peroxy-monosulfate activation to degrade sulfamethoxazole efficiently. *Chem. Eng. J.* **474**, 145973 (2023).
42. Zhou, X. et al. Identification of Fenton-like active Cu sites by heteroatom modulation of electronic density. *Proc. Natl Acad. Sci. USA* **119**, 2119492119 (2022).
43. Mi, X. et al. Facilitating redox cycles of copper species by pollutants in peroxy-monosulfate activation. *Environ. Sci. Technol.* **56**, 2637–2646 (2022).
44. Xu, S. et al. Highly efficient peroxy-monosulfate activation on electron-enriched ruthenium dual-atom sites catalysts for enhanced water purification. *Adv. Funct. Mater.* **33**, 2308204 (2023).
45. Wu, Z. et al. Active center size-dependent Fenton-like chemistry for sustainable water decontamination. *Environ. Sci. Technol.* **57**, 21416–21427 (2023).
46. Illas, F. Fundamental concepts in heterogeneous catalysis. *Angew. Chem. Int. Ed.* **54**, 10404–10405 (2015).
47. Maintz, S., Deringer, V. L., Tchougreeff, A. L. & Dronskowski, R. Analytic projection from plane-wave and PAW wavefunctions and application to chemical-bonding analysis in solids. *J. Comput. Chem.* **34**, 2557–2567 (2013).
48. Deringer, V. L., Tchougreeff, A. L. & Dronskowski, R. Crystal orbital Hamilton population (COHP) analysis as projected from plane-wave basis sets. *J. Phys. Chem. A* **115**, 5461–5466 (2011).
49. Chen, C. et al. Single-atom co sites confined in layered double hydroxide for selective generation of surface-bound radicals via peroxy-monosulfate activation. *Appl. Catal. B Environ.* **340**, 123218 (2024).
50. Wang, J. et al. Pilot-scale advanced treatment of actual high-salt textile wastewater by a UV/O<sub>3</sub> pressurization process: evaluation of removal kinetics and reverse osmosis desalination process. *Sci. Total Environ.* **857**, 159725 (2023).
51. Lu, T. A comprehensive electron wavefunction analysis toolbox for chemists, Multiwfn. *J. Chem. Phys.* **161**, 082503 (2024).
52. Lu, T. & Chen, F. Multiwfn: a multifunctional wavefunction analyzer. *J. Comput. Chem.* **33**, 580–592 (2012).
53. Gong, Y. et al. Whose oxygen atom is transferred to the products? A case study of peracetic acid activation via complexed Mn<sup>II</sup> for organic contaminant degradation. *Environ. Sci. Technol.* **57**, 6723–6732 (2023).

54. Chen, X. J. et al. pH-driven efficacy of the ferrate(VI)-peracetic acid system in swift sulfonamide antibiotic degradation: a deep dive into active species evolution and mechanistic insights. *Environ. Sci. Technol.* **57**, 20206–20218 (2023).
55. Zhang, H., Lee Smith, R., Guo, H. & Qi, X. Cobalt cross-linked ordered mesoporous carbon as peroxymonosulfate activator for sulfamethoxazole degradation. *Chem. Eng. J.* **472**, 145060 (2023).
56. He, J. et al. The enhanced catalytic degradation of sulfamethoxazole over Fe@nitrogen-doped carbon-supported nanocomposite: Insight into the mechanism. *Chem. Eng. J.* **439**, 135784 (2022).
57. Zhang, A. et al. Motivation of reactive oxygen and nitrogen species by a novel non-thermal plasma coupled with calcium peroxide system for synergistic removal of sulfamethoxazole in waste activated sludge. *Water Res.* **212**, 118128 (2022).
58. Du, J. et al. Hydroxyl radical dominated degradation of aquatic sulfamethoxazole by Fe<sup>0</sup>/bisulfite/O<sub>2</sub>: kinetics, mechanisms, and pathways. *Water Res.* **138**, 323–332 (2018).
59. Wu, J. H. et al. Tailoring the selective generation of oxidative organic radicals for toxic-by-product-free water decontamination. *Proc. Natl Acad. Sci. USA* **121**, e2403544121 (2024).
60. Perdew, J. P., Burke, K. & Wang, Y. Generalized gradient approximation for the exchange-correlation hole of a many-electron system. *Phys. Rev. B* **54**, 16533–16539 (1996).

## Acknowledgements

The authors thank the National Natural Science Foundation of China (52270149, 51908528, 52192684, and 51821006) and Fundamental Research Funds for the Central Universities grant (2024IAIS-QN013, 2021CDJQY-014) for supporting this work. The authors would like to thank the related characterizations from Shiyanjia Lab ([www.shiyanjia.com](http://www.shiyanjia.com)).

## Author contributions

F. Chen and Z. Q. Zhang conceived and planned the experiments. Z. Q. Zhang performed the relative experiments. P. J. Duan performed the theoretical calculations. J. X. Zheng and Y. Q. Xie assisted in the experimental study, and P. J. Duan, C. W. Bai, Y. J. Sun, X. J. Chen, and F. Chen assisted in analyzing various characterizations. Z. Q. Zhang and P. J. Duan wrote the initial draft, F. Chen and H. Q. Yu further modified the manuscript.

## Competing interests

The authors declare no competing interests.

## Additional information

**Supplementary information** The online version contains supplementary material available at <https://doi.org/10.1038/s41467-024-55622-y>.

**Correspondence** and requests for materials should be addressed to Fei Chen or Han-Qing Yu.

**Peer review information** *Nature Communications* thanks Qixing Zhou and the other, anonymous, reviewers for their contribution to the peer review of this work. A peer review file is available.

**Reprints and permissions information** is available at <http://www.nature.com/reprints>

**Publisher's note** Springer Nature remains neutral with regard to jurisdictional claims in published maps and institutional affiliations.

**Open Access** This article is licensed under a Creative Commons Attribution-NonCommercial-NoDerivatives 4.0 International License, which permits any non-commercial use, sharing, distribution and reproduction in any medium or format, as long as you give appropriate credit to the original author(s) and the source, provide a link to the Creative Commons licence, and indicate if you modified the licensed material. You do not have permission under this licence to share adapted material derived from this article or parts of it. The images or other third party material in this article are included in the article's Creative Commons licence, unless indicated otherwise in a credit line to the material. If material is not included in the article's Creative Commons licence and your intended use is not permitted by statutory regulation or exceeds the permitted use, you will need to obtain permission directly from the copyright holder. To view a copy of this licence, visit <http://creativecommons.org/licenses/by-nc-nd/4.0/>.

© The Author(s) 2024